First World Congress on Condition Monitoring (WCCM 2017), London, 13-16 June 2017

Fault detection of bearing defects for ballscrew based electro-mechanical actuators

Mohamed A A Ismail and Jens Windelberg
DLR – (German Aerospace Center), Institute of Flight Systems
38108 Braunschweig, 38108, Germany
+49-531-295-2734
Mohamed.Ismail@dlr.de
Jens.Windelberg@dlr.de

Abstract

Electro-mechanical actuators (EMAs) are considered a promising energy-efficient technology for actuating flight controls of future aircrafts. When it comes to aerospace systems, the EMAs degradation should be checked in regular maintenance events or through condition-based maintenance. Ball bearings have a significant failure rate for flight control EMAs and they are usually monitored by vibration noise. A challenge for detecting bearing faults, using state-of-the-art industrial methods, is the presence of a ballscrew mechanism that produces a nominal vibration noise similar to that of faulty bearings. No prior research has investigated this problem. This paper explores vibration noises generated from a set of healthy and faulty bearings included in a typical ballscrew EMA. In addition, a method is introduced for evaluating fault diagnosis performance for different time and frequency vibration features. The technique has been validated on an EMA actuator at the German Aerospace Center (DLR).

1. Introduction

More-electric aircraft (MEA) have gained in popularity as a development toward making future aircraft more economical and environmentally friendly. Flight control surfaces (e.g., aileron, rudder) of current commercial aircraft are based on hydraulic actuators (HAs). HAs are heavy and energy inefficient, leading to additional fuel consumption; however, they have very reliable features, e.g. fail-safe that provide superior safety in air transportation [(1)].

Within the scope of MEA, electro-mechanical actuators (EMAs) are replacing hydraulic actuators to minimize the aforementioned deficiencies [(2)]. A generalized EMA design may consist of an electric motor, a set of bearings, a gearbox, and an actuation mechanism such as a ballscrew or rollerscrew [(3)]. Here, we focus on ballscrew-based EMAs because they are more popular for in-service EMA such as the actuating horizontal stabilizer of the Airbus 380 and the roll spoilers of the Boeing 787 [(4)].

However, a significant design challenge of EMA is limited reliability resulting from several interfering sub-components (i.e., bearings, gears, and ball screw). This may introduce new (relative to HAs) failure risks in actuation systems, such as excessive wear,

pitting/spalling, and actuator jamming [1–4]. Some of these failures have relatively slow progression rates in the form of in-service degradation, which can be monitored during routine pre-flight checks, the target scenario for this work. Examples of this scenario have been cited for EMA gear faults [2] and for ballscrew faults [5].

Bearing faults, in general, are responsible for about 40% to 50% of flight-control EMA mechanical failures [3]. The present paper describes an investigation conducted into the problem of vibration-based detection of bearing faults (i.e., localized spalls) in the presence of a ballscrew mechanism. The current state-of-the-art fault diagnosis methods for spalled bearings rely on identifying specific fault frequencies in the time domain (e.g., ball pass inner race frequency). The interference of ballscrew vibrational noise with the ability to diagnose faults in bearings has not been cited in determinations of fault diagnosis difficulties. This problem is crucial for EMA health monitoring for aerospace as well as industrial applications.

The paper is organized as follows. In Section 2, the vibration response for ball bearings and ballscrews is summarized. In Section 3, a method to evaluate fault diagnosis opportunities is presented. Section 4.1 provides a description of the actuator test stand, sensors, and seeded fault scenarios. Finally, Section 4.2 discusses the experimental results of the fault diagnosis approach described in Section 3.

2. Problem investigation

This section describes essential vibration features for ball bearings and ballscrews. These features will be used later to explore opportunities for fault detection of faulty bearings attached to a ballscrew EMA.

2.1 Vibration response of ball bearings

The normal operation of a ball bearing can be monitored by an accelerometer mounted close to the bearing, as shown in Figure 1. The accelerometer measures the vibrations of the case; in the absence of bearing faults, the signal looks similar to that shown in Figure 1. There are no specific high-frequency excitations, and any discrete low-frequency components may be attributed to rotor-related problems, such as improper balance or a misalignment of the rotating shaft. A localized spall fault at one of the bearing elements imposes a periodic disturbance on the rotating shaft. This disturbance is due to the successive passages of the balls over the spall, which create a series of impact forces that excite the bearing sub-components and the attached assembly [6].

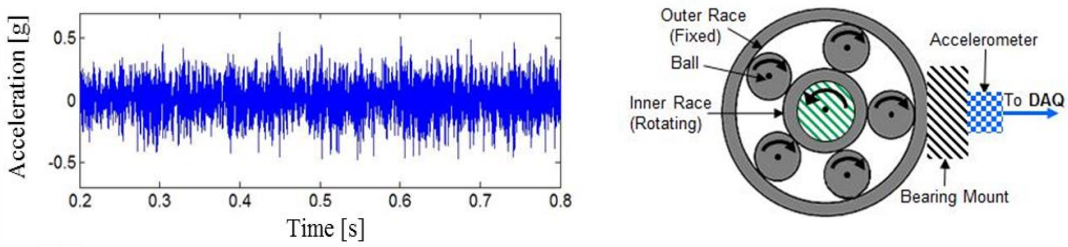

Figure 1. Vibration measurements for a healthy bearing through a basic instrumentation setup of an accelerometer fixed on the bearing mount

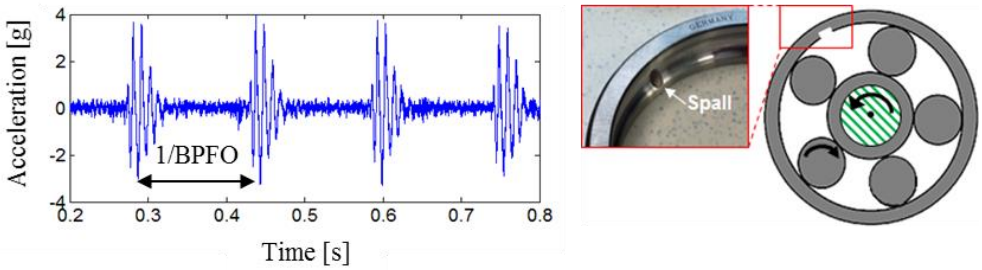

Figure 2. An outer-race spall and the corresponding acceleration measurements: the *FCF* is the BPFO. The balls' motion is disturbed in the spalled zone, inducing four vibration spikes

A series of vibrational transients in the vibration data indicates the occurrence of a spall, as shown in Figure 2. These transients occur at a unique fault characteristic frequency (*FCF*), which is a function of the spall location (i.e., at the inner race, the outer race, or a ball), the operating speed N in Hertz, the bearing geometry, and the load angle. For example, the ball-pass frequency for the outer race (BPFO) is the *FCF*, which indicates a spall in the outer race in Eq. (1). For an inner-race spall, the *FCF* is the ball-pass frequency for the inner race (BPFI) in Eq. (2). The equations for calculating these *FCFs* are as follows [6]:

$$\boldsymbol{BPFO = \frac{NB}{2}\left(1 - \frac{D_b}{D_p}\cos\alpha\right), \text{and}} \tag{1}$$

$$\boldsymbol{BPFI = \frac{NB}{2}\left(1 + \frac{D_b}{D_p}\cos\alpha\right),} \tag{2}$$

where N is the shaft speed in Hertz, B is the number of balls, D_b[mm] is the ball diameter, D_p[mm] is the bearing pitch diameter, and α[Deg] is the contact (load) angle of the bearing.

2.2 Vibration response of the ballscrew mechanism

The ballscrew mechanism is an essential component of the EMA that is used to convert rotational motion ω delivered by an electric motor into a translation motion to drive a a flight control surface. The ballscrew consists of four main parts: the screw, the nut, the balls, and the recirculation channel, as shown in Figure 3.

During nominal operation, the balls' movement takes place in two zones: loaded and unloaded. The loaded zone is the helical groove of the screw, where the ball is subjected to axial and radial forces. The unloaded zone is where the ball passes through the recirculating channel (also known as the return channel).

The tongue forces the balls to change their smooth helical path into the recirculating channel path. Consequently, each ball entering the recirculating channel generates significant impact force on the tongue. Because the tongue is attached to the nut and its edge is very close to the nut's inner surface, the impact frequency of tongue–ball approximately equals the ball–nut passing frequency f_{bn} as investigated in [5] and represented by Eq. (3).

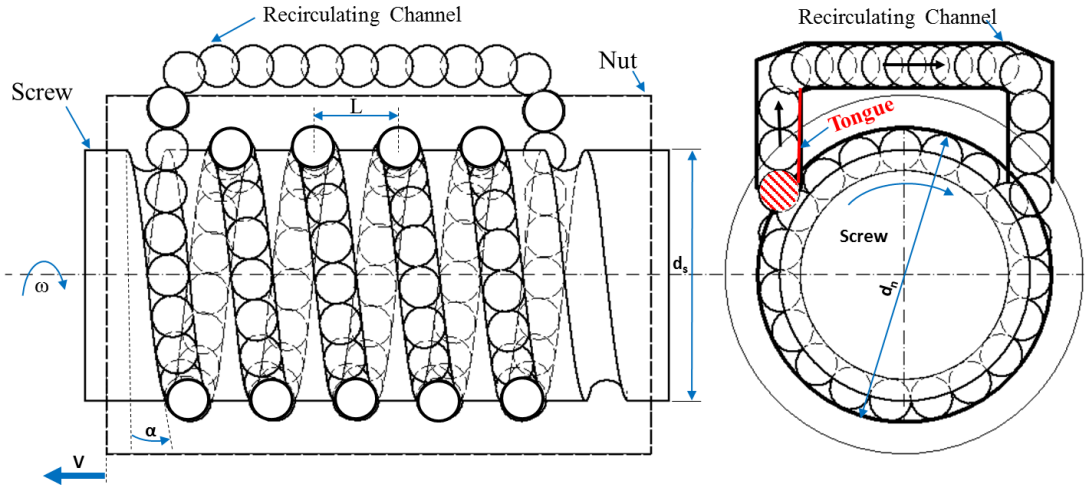

Figure 3. Elements of a ballscrew mechanism: screw, nut, balls, and return channel

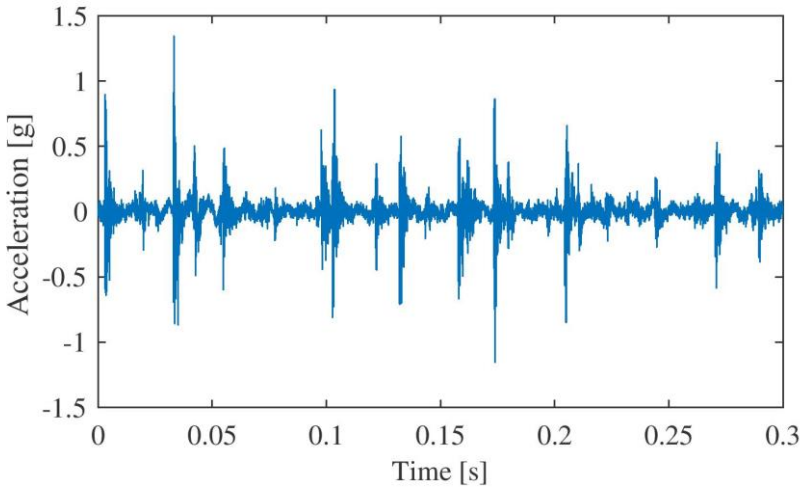

Figure 4. Vibration response of a healthy ballscrew in an EMA. The spikes are separated on average by $1/f_{bn}$ because of partial irregular movement of the balls

$$f_{bn} = \frac{f\,B\cos\alpha_o}{1+\frac{(1+\delta\cos\alpha_o)}{(1-\delta\cos\alpha_o)}}, \tag{3}$$

where B is the number of balls in a revolution or along the screw lead, f_{bn} is the ball-passing frequency with regard to a fixed point on the nut, and f is the screw shaft rotation in rps. α_0 is screw load angle, and δ is the ratio between the ball diameter and screw pitch diameter. A detailed derivation of Eq. (3) can be found in [5].

A more detailed analysis of Figure 4 can be obtained by using a signal spectrogram as depicted in Figure 5. The healthy vibration signature induced by tongue impacts are indicated by vertical lines separated on average by f_{bn}. Significantly, the frequency content of these spikes extends over nearly the full bandwidth of the signal.

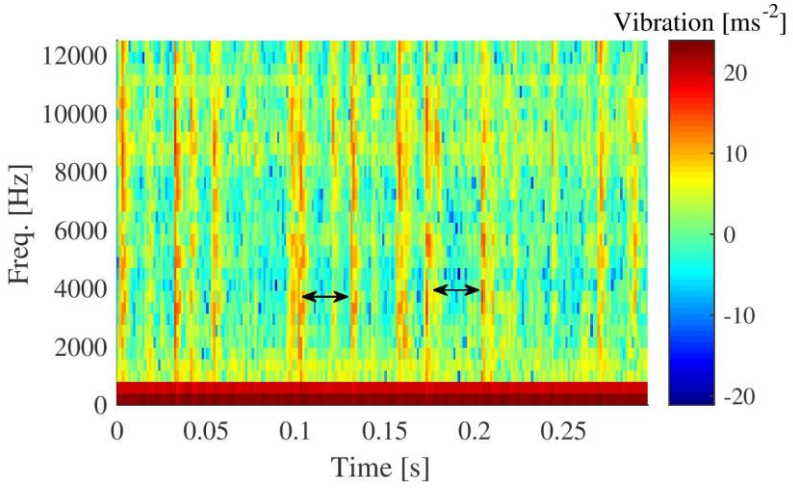

Figure 5. Spectrogram of Figure 4 with 20% of EMA rated load. Examples of tongue spikes f_{bn} are depicted by two double-headed arrows

2.3 Summary

Ball bearings produce only a unique vibration signature corresponding to a specific fault; in contrast, the ballscrew mechanism produces a vibration signature corresponding to a design element (return channel) that is independent of ballscrew health. This signature may be similar to that of a faulty bearing. In the following sections, the effectiveness of well-known diagnosis features for ball bearings are evaluated with the presence of a healthy EMA ballscrew.

3. An approach to evaluating fault diagnosis

3.1 Diagnosis features

Three sets of time and frequency features are used for characterizing the vibration response of an EMA in order to classify nominal and faulty bearings as follows.

3.1.1 Time features

Time features provide a direct evaluation of the signal characteristics without focusing on specific frequency content. This group involves three features: root-mean square (RMS) of the signal, signal kurtosis, and peak-to-peak of the signal waveform. It has been demonstrated that the signals from EMA sensors may involve a non-linear trend, which may bias the time features. A pre-whitening detrending technique using a second-order linear AR filter, similar to that described in [7], has been used as a pre-processing step to minimize possible trends.

3.1.2 Power spectrum density features

Power spectrum density (PSD) is a popular tool for identifying the energy distribution of the signal over its full bandwidth. Extracting specific features for PSD is challenging as PSD involves a wide spectrum that may belong to nearby vibration sources and background noise. Here, we propose representing PSD information by considering three features: PSD level, PSD minimum, and PSD width as shown in Figure 6. Welch's PSD estimator has been used with a fixed window length of 256 samples and an overlap ratio of 50%.

3.1.3 Spectral kurtosis features

Spectral kurtosis provides another approach that focuses on a narrow frequency band. This band is expected to have the highest useful signal-to-noise ratio (SNR). The selection of such band relies on dividing the whole spectrum of the signal into overlapped frequency levels as shown in Figure 7. The optimum band has been selected based on the highest kurtosis. Here, we utilize an efficient spectral kurtosis algorithm, the fast kurtogram [8], as shown in Figure 8.

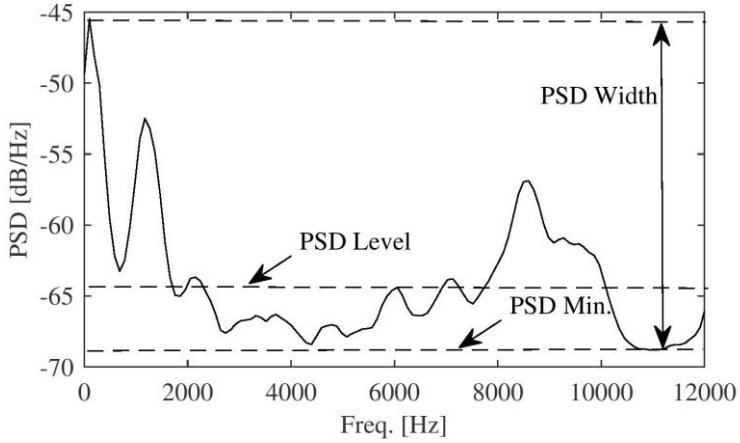

Figure 6. Example of locating PSD features: the PSD level is the average of the whole spectrum, the PSD minimum is the lowest PSD value, and the PSD width is the PSD bounds

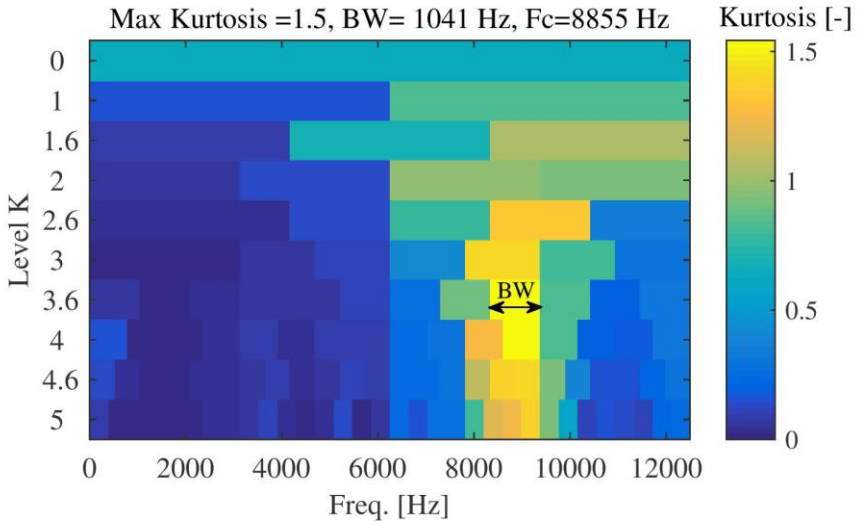

Figure 7. Example of kurtogram features: carrier frequency "Fc" for optimum frequency band where selected bandwidth "BW" has the highest kurtosis. Y-axis, Level *K* indicates 2^k frequency division levels for filter banks

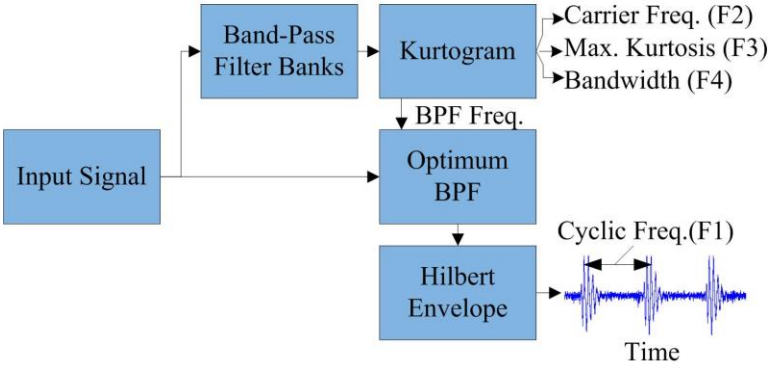

Figure 8. Calculation of spectral kurtosis features (F1–F4) using a set of band pass filters (BPFs) within the kurtogram and Hilbert envelope

The kurtogram estimates the optimum band of the signal with max kurtosis. Furthermore, an additional feature is evaluated: the cyclic frequency that is included in this band. Cyclic frequency is a generalized term for FCF in Eqs. (1)–(3), as shown in Figure 3, and can be extracted by applying a Hilbert envelope as in Figure 7.

3.2 Performance metrics

Two performance metrics are proposed to evaluate diagnosability: separability and coverage. Separability is the minimum change of the feature magnitude from the healthy condition to the faulty condition as a percentage. The separability is a dimensionless ratio that correlates with the feature's sensitivity to detect any signs of abnormality, as shown in Figure 9. Higher separability ratios are desired in order to increase the certainty of fault detection. In the case of a feature for which a threshold between healthy and faulty levels cannot be assigned, the separability is set to zero. The coverage is the percentage of the operating conditions at which the feature has non-zero separability. Examples for calculating coverage are depicted in Figure 10.

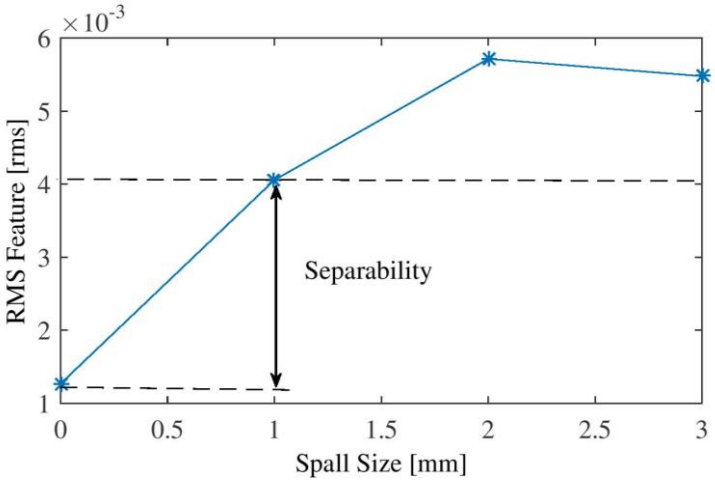

Figure 9. An example of calculating separability for the RMS feature for spall faults. At healthy condition (zero spall), the RMS feature is 1.2×10^{-3} and at the nearest faulty case (at 1 mm spall), the feature is 4.0×10^{-3}; thus, the separability equals 233%

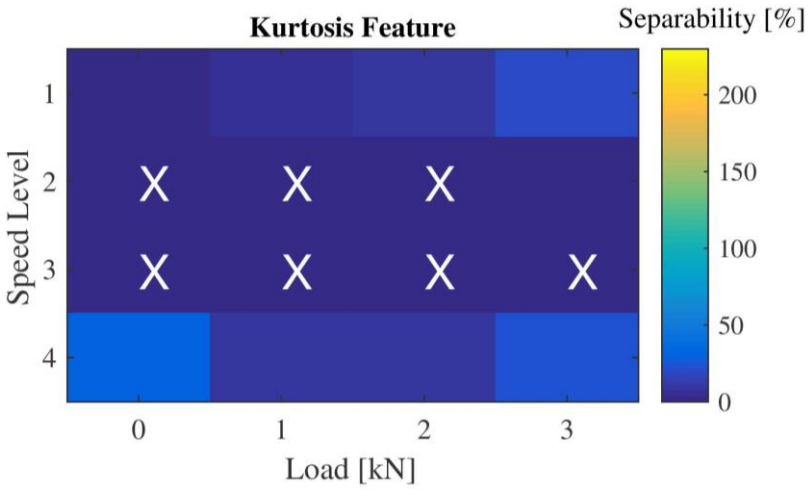

Figure 10. Coverage example, where there are seven conditions at which the feature cannot separate healthy from faulty condition; thus, the coverage is 7/16 or 44%

4. Experimental work

4.1 Test stand and data description

A direct-drive EMA with a rotating nut ballscrew is considered for the experimental work. The test stand comprises an EMA driven by a three-phase permanent magnet synchronous motor, a hydraulic actuator to apply axial load similar to flight control surfaces, data acquisition (DAQ), and PID controller based on the dSPACE platform. Three types of sensors have been considered for health monitoring purposes, namely, six accelerometers (PCB 352C65), four ultrasound vibration sensors (Ultra-track 750), and a hall effect current sensor (LEM LAH25NP). The ultrasound sensor has a narrow working bandwidth of 38–42 kHz, which is demodulated to 0–6 kHz by the embedded electronic circuit.

The measurements are initially filtered using the anti-aliasing eighth-order Butterworth filter with a cut-off frequency of 10 kHz; then they are sampled at a 16 bit and 25 kHz sampling rate. The locations of the sensors and a schematic of the setup are shown in Figure 11. The setup can generate different load and position profiles. Here, constant speed and load profiles are used, which can be pre-defined for a pre-flight check. They include four load levels (0, 1, 2, 3) kN and four speed levels (120, 360, 600, 720) rpm.

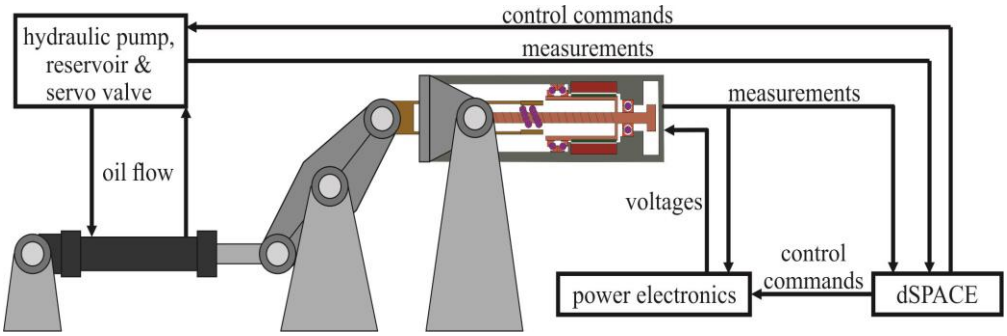

Figure 11. (a) Schematic of the EMA setup emulating an aileron

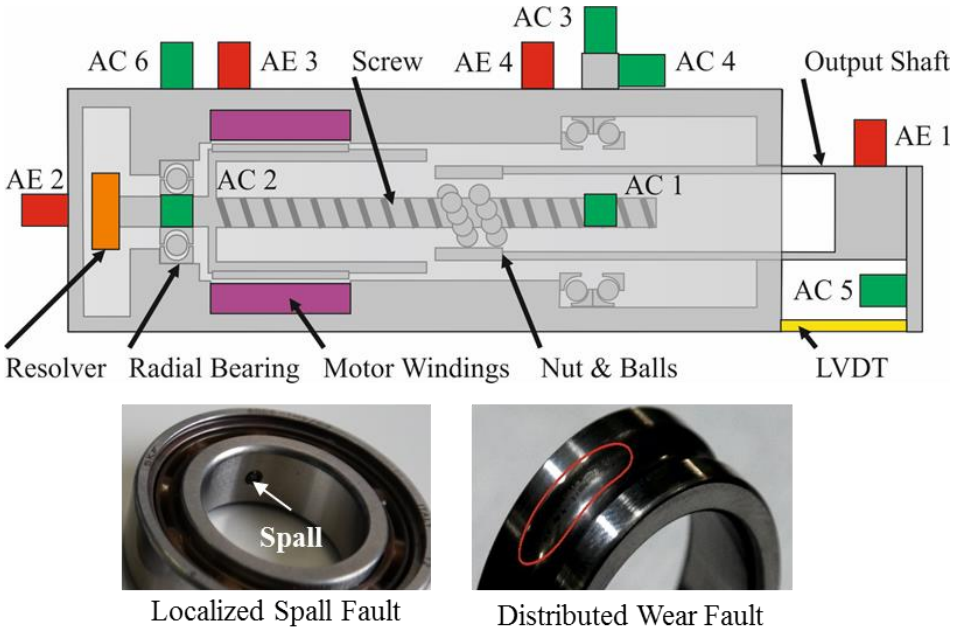

Figure 11. (b) Sensor locations on the EMA and radial bearing faults, where AC denotes accelerometer and AE denotes ultrasound. AC1 and AC2 are placed on the EMA housing.

Deep groove ball bearings (SKF 6005) were seeded with two fault types: a localized spall at the bearing outer/inner races and distributed wear over the races. The spall was manufactured using a drill tool with three diameters (1, 2, and 3 mm to create hollow cuts), while wear fault was seeded by adding abrasive particles to the bearing lubricant.

4.2 Results and discussion

As an initial step, the problem of detecting a faulty bearing based on *FCFs* is visualized in Figure 12. The close cyclic frequencies between the healthy and faulty datasets demonstrate the need to search for other features to reliably identify faulty conditions.

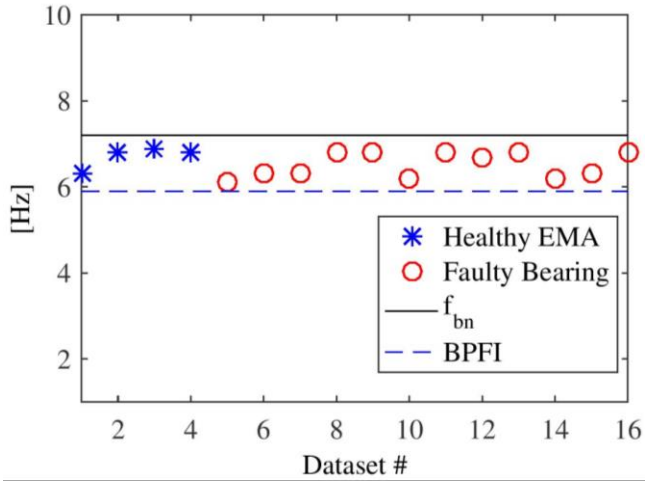

Figure 12. Cyclic frequencies for some of the healthy and faulty datasets are the average ballscrew frequency, f_{bn} from Eq. (3) and BPFI from Eq. (2). Both f_{bn} and BPFI have close values, interfering with fault detection

The investigated features in Section 3 are evaluated here for the purpose of detecting seeded faults. There are 124 datasets consisting of 26% healthy and 74% faulty scenarios of bearing wear and inner and outer spalls. Each dataset involves 11 sensors, with 110 features per dataset as in Figure 13.

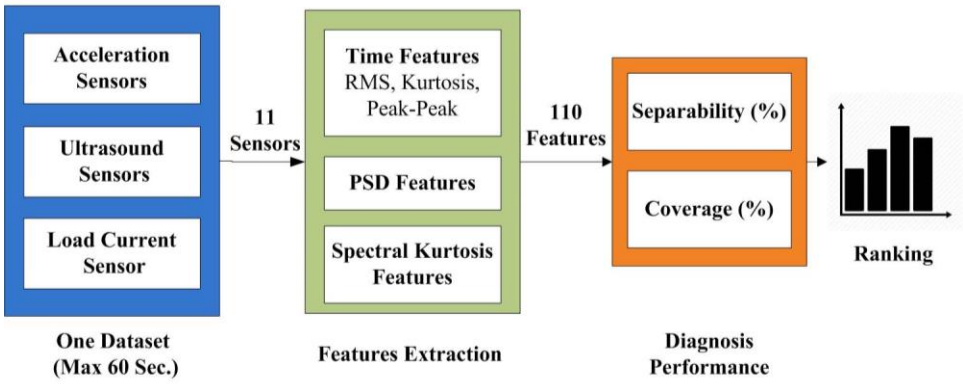

Figure 13. Signal flow for evaluating fault detection and classification capabilities of different sensors and features

A total of 124*110=13,640 features are evaluated based on their separability and coverage scores. The evaluation results are depicted in Figure 14. The maximum coverage scores of 100% are observed for ultrasound sensor no. 2 (pre-whitened RMS feature) and accelerometer no. 5 (PSD level feature). Their average separability levels are 137% and 101%, respectively. Ultrasound no.2 is the nearest ultrasound sensor to faulty radial bearing considering less disturbance noise from the motor windings. Accelerometer no. 5 is mounted directly on the EMA output shaft, at which significant amount of vibration noise has been acquired directly on the load path of the actuator; while all other accelerometers are mounted on external multi-layer housing.

In contrast, the best phase current feature is kurtosis, which has a coverage score of 81% and only 2.7% average separability. Such very low separability may intersect with other operating conditions or factors such as thermal deviation and overload safety margin, which is typically 5–10% for electrical motors.

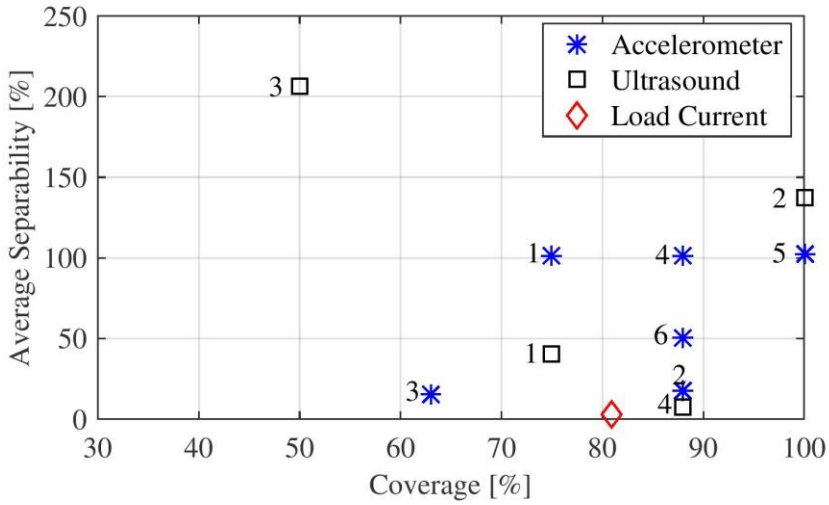

Figure 14. Overall results for all faults and all sensors

The low coverage of phase current and other sensors may be influenced by two factors: 1) high level of ballscrew noise dominates the overall vibration noise of the EMA, and 2) sensor locations at which the signal is almost damped or absorbed by the EMA housing.

The detailed results for ultrasound no. 2 and accelerometer no. 5 are depicted in Figures 15 and 16. The ultrasound feature is primarily influenced by operating speed. Higher separation between healthy and faulty is an attribute of lower running speeds, while the accelerometer feature is primarily influenced by high speed level with a minor contribution to the load. This is common for accelerometers because vibration energy is proportional to operating speed.

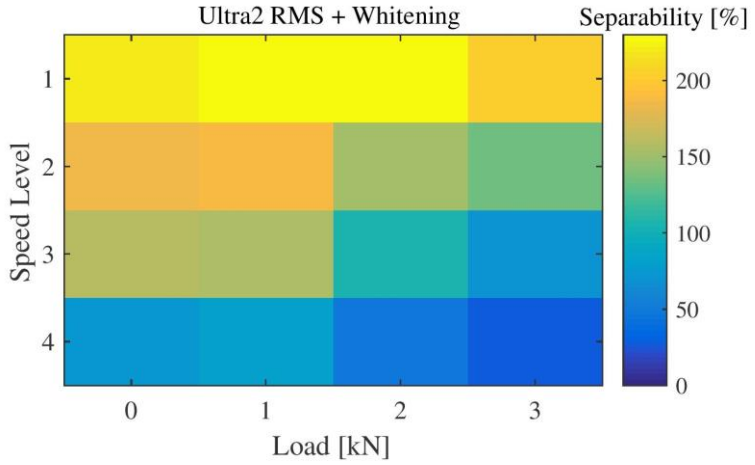

Figure 15. Separability for load-speed levels for ultrasound 2

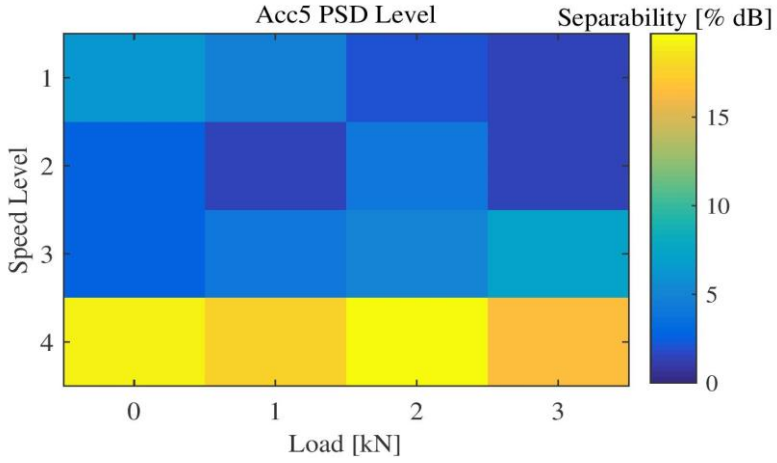

Figure 16. Separability for different load-speed for accelerometer 5

5. Conclusion

An investigation showed that ballscrews produce a vibration noise induced by a design element (the ball return channel) that is independent of the health of the ballscrew or the actuator. This noise has a cyclic frequency modulated by a wideband carrier and may mask vibration noise generated by faulty bearings. In addition, fault detection

performance was evaluated via three sensing technologies: accelerometers, ultrasound, and phase current. The best sensors are an accelerometer (PSD level feature) and an ultrasound sensor (pre-whitened RMS feature). Both of these achieve coverage scores of 100% for 16 different operating conditions with separability levels higher than 100%. The best phase current feature has a coverage score of 81% and a low separability of 2.7%. The low coverage can be interpreted as a high level of ballscrew noise and sensor location. Future work is planned to evaluate bearing fault quantification challenges to support prognosis-based maintenance.

Acknowledgement

This work is partially supported by the OMAHA project through the German national aerospace research program (Lufo V-1).

Supported by:

on the basis of a decision
by the German Bundestag

6. References

[1] J. A. Rosero, J. A. Ortega, E. Aldabas, and L. Romeral, "Moving Towards a More Electric Aircraft," *IEEE Aerosp. Electron. Syst.*, vol. 22, no. 3, pp. 3–9, Mar. 2007.

[2] Legrand, M.-O., 2016. *ACTUATION2015(Modular Electro Mechanical Actuators ACARE 2020 Aircraft and Helicopters*. Final Report, www.actuation2015.eu.

[3] D. S. Bodden, N. S. Clements, B. Schley, and G. Jenney, "Seeded Failure Testing and Analysis of an Electro- Mechanical Actuator"," *IEEE Aerospace conference*. Big Sky, USA, March, 2007.

[4] S. Narasimhan, I. Roychoudhury, E. Balaban, and A. Saxena, "Combining Model-Based and Feature-Driven Diagnosis Approaches – A Case Study on Electromechanical Actuators," *21st International Workshop on Principles of Diagnosis*, 2010, Portland, USA

[5] M. A. A. Ismail, E. Balaban, and H. Spangenberg, "Fault detection and classification for flight control electromechanical actuators," *IEEE Aerospace Conference*, Big Sky, USA, March, 2016.

[6] R. B. Randall and J. Antoni, "Rolling element bearing diagnostics-A tutorial," *Mech. Syst. Signal Process.*, vol. 25, no. 2, pp. 485–520, 2011.

[7] R. B. Randall and N. Sawalhi, "A comparison of methods for separation of deterministic and random signals," *Int. J. Cond. Monit.*, vol. 1, no. 1, pp. 11–19, 2011.

[8] J. Antoni, "Fast computation of the kurtogram for the detection of transient faults," *Mech. Syst. Signal Process.*, vol. 21, no. 1, pp. 108–124, 2007.